Chapter 5

Digital generation of coherence vortices

This chapter explores a novel approach for digitally generating coherence vortices using two cutting-edge devices: a digital micromirror device (DMD) and a spatial light modulator (SLM). The methodology is thoroughly explained, supported by a comprehensive theoretical foundation and detailed descriptions of the experimental setups. These digital platforms enable precise control over the generation process, offering flexibility and scalability in creating coherence vortices for advanced optical applications.

5.1 Introduction

Singular optics has attracted increasing attention in recent years due to a promising source for novel technologies. The traditional focus of singular optics is on the analysis of coherent optical fields with a phase singularity and a doughnut amplitude structure around the singular point. The phase singular beams are commonly referred to as optical vortices [276, 277]. Originating from the helicoidal spatial wavefront surrounding the phase singularity, it exhibits a topological structure on its wavefront with a topological charge (TC) l. Allen et al. in 1992 highlighted that an optical vortex beam, carry quantized orbital angular momentum (OAM), with $l\hbar$ per photon [19]. The diverse properties of optical vortices find utility in various applications, such as optical tweezers [94, 95], optical communication and data storage [96-99], microscopy imaging [8] etc. Several techniques have been proposed for generating vortex beams, the most direct method is to let the light beam propagate into a medium with spiral inhomogeneity, creating an integer phase step along the azimuthal angle [24, 25]. The other common techniques involve mode converter (cylindrical lens) [27-29], computer-generated holograms [37-39], controllable mirrors [309], three beam interference [310] etc.

While coherent beams have traditionally been a major focus of interest, light with low coherence has also garnered significant attention due to its unique properties and applications. In Chapter 4, we provided a comprehensive discussion on the history of vortices in low-coherence light, known as coherence vortices (CVs), highlighting their advantages and diverse applications. Recent advancements in spatial light modulator (SLM) technologies and digital micromirror devices (DMDs) have further transformed the field, enabling the precise generation and control of arbitrary optical fields, including those with CVs. Recent studies have demonstrated the digital generation of vortices in partially coherent light through the use of SLMs [291, 311]. SLMs are advanced electro-optical

devices designed to control and modify fundamental properties of light, such as its amplitude, phase, and polarization. They consist of pixelated displays containing hundreds of thousands of liquid crystals (LC) filled cells. Each pixel in the SLM corresponds to an individually addressable LC cell placed between transparent electrodes. A phase-type SLM based on the voltage-controlled manipulation of LC molecules to modulate the phase of incident light. By varying the voltage applied to the transparent electrodes, the LC molecules reorient, altering the local refractive index and consequently the phase of light passing through. The SLM operates by displaying grayscale images, where the intensity of each pixel in the image corresponds to the voltage applied to the respective LC cell. This grayscale voltage control enables precise phase modulation across the wavefront [32, 312]. The periodic spacing between the pixels of the SLM acts as a diffraction grating, leading to the generation of multiple diffraction orders. Fig. 5.1 (a) shows different diffraction orders through SLM. Where the 0^{th} order shows the undiffracted light that passes straight through the SLM without experiencing modulation. +1 and -1 are the first diffraction orders and +2, -2, +3, -3… are higher diffraction orders.

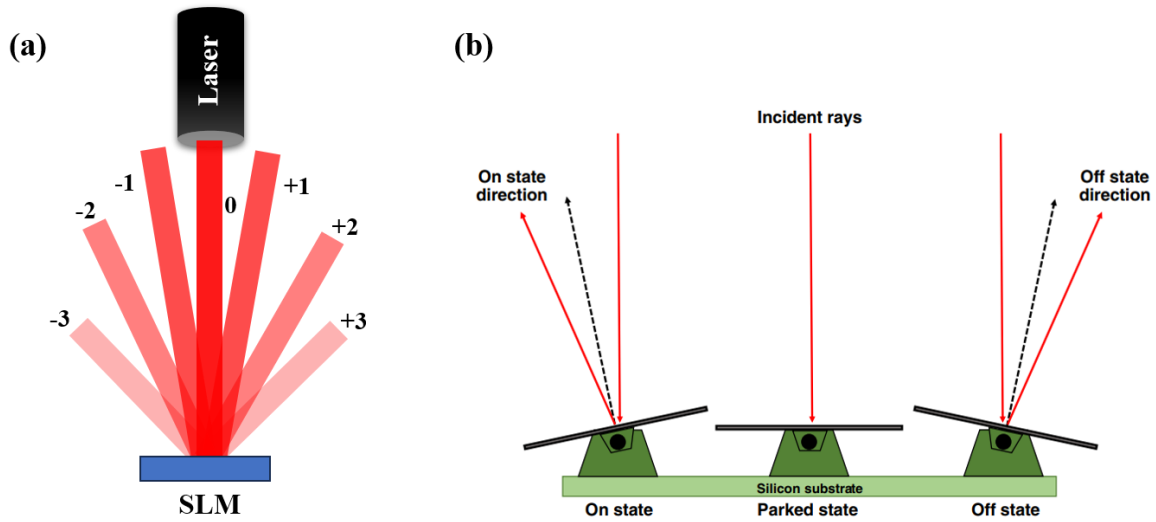

Fig. 5.1 (a) Schematic diagram of light diffracted through SLM (b) The three possible mirror states in DMD: on, parked, and off [18].

DMDs, on the other hand, consists of an array of individually addressable micromirrors, each mounted on a hinge that enables them to pivot between different states suitable for the amplitude modulation of light. These states include the "on" state, where the mirror is tilted to reflect light in a desired direction; the "off" state, where it reflects light away from the intended path; and the "parked" state, which is nominally parallel to the protective glass sheet but only occurs when the device is powered off. The three possible mirror states are represented in Fig. 5.1 (b). Each micromirror acts as a binary switch, contributing to or excluding its portion of the light beam based on its state. This mechanism allows the DMD to project or modulate light with high speed and precision. Their fast-switching rates and polarization insensitivity make them an attractive tool for shaping light [313, 314].

In this paper, we present a method for generating CVs within the two-point correlation function using these advanced devices. Unlike static, fabricated devices, SLMs and DMDs are fully reconfigurable, offering the advantage of being rewritable and thus highly versatile. This capability enhances their potential for exploring new optical phenomena and applications, providing a flexible platform for creating dynamic and customizable optical fields. This study explores two distinct approaches for generating CVs in the two-point correlation function using advanced digital devices, namely the DMD and the SLM. In the first approach, binary pinhole patterns are displayed on the DMD, and the reflected light modulated by these patterns enables the formation of CVs in the two-point correlation function. This method efficiently utilizes the binary control of the DMD to achieve precise spatial modulation. In the second approach, a helical phase profile is projected onto the SLM, leveraging the polarization basis of light. One orthogonal polarization component of the incident transversely polarized light interacts with the SLM, encoding the helical phase profile into it. The other polarization component remains

unaffected and directly reaches the detector. In addition to CVs with integral topological charges, CVs with fractional *i.e.*, non-integral topological charges are also generated.

5.2 Digital generation using DMD

In this section, we show generation of CVs using binary pinhole plates projected on DMD. The detailed theoretical basis, experimental design and results are discussed in the upcoming sections.

5.2.1 Theoretical basis

Fig. 5.2 represents the principle behind our proposed technique. The two-point correlation function at the DMD plane is given by

$$W_\lambda(\mathbf{v}_1, \mathbf{v}_2) = \langle U_\lambda^*(\mathbf{v}_1) U_\lambda(\mathbf{v}_2) \rangle \tag{5.1}$$

where $\langle \quad \rangle$ represents the ensemble average and λ is the wavelength.

A single realization of the field at the far-field is represented as

$$U_\lambda(\boldsymbol{r}) = \int U_\lambda(\mathbf{v})\, exp\left(-i\frac{2\pi}{\lambda f}\mathbf{v}.\boldsymbol{r}\right) d^2\mathbf{v} \tag{5.2}$$

where f is the focal length of the Fourier transforming lens L. Thus, the far-field two-point correlation function is represented as

$$W_\lambda(\boldsymbol{r}_1, \boldsymbol{r}_2) = \iint \langle U_\lambda^*(\mathbf{v}_1) U_\lambda(\mathbf{v}_2) \rangle\, exp\left[-i\frac{2\pi}{\lambda f}(\mathbf{v}_2.\boldsymbol{r}_2 - \mathbf{v}_1.\boldsymbol{r}_1)\right] d^2\mathbf{v}_2 d^2\mathbf{v}_1 \tag{5.3}$$

For an incoherent source,

$$\langle U_\lambda^*(\mathbf{v}_1) U_\lambda(\mathbf{v}_2) \rangle = I_\lambda(\mathbf{v})\delta(\mathbf{v}_2 - \mathbf{v}_1) \tag{5.4}$$

where $I(\mathbf{v})$ is the source intensity and δ represents the two-dimensional Dirac delta function. Therefore, Eq. (5.3) becomes

$$W_\lambda(\boldsymbol{r}_1, \boldsymbol{r}_2) = \int I_\lambda(\mathbf{v}) exp\left[-i\frac{2\pi}{\lambda f}(\boldsymbol{r}_2 - \boldsymbol{r}_1).\mathbf{v}\right] d^2\mathbf{v} \tag{5.5}$$

If the incoherent light possesses a finite spectral bandwidth, the corresponding two-point correlation function must be evaluated as an integral across the entire wavelength range covered by the spectrum

$$W(\boldsymbol{r}_1, \boldsymbol{r}_2) = \int \left\{ \int I_\lambda(\mathbf{v}) exp\left[-i \frac{2\pi}{\lambda f} (\boldsymbol{r}_2 - \boldsymbol{r}_1).\mathbf{v} \right] d^2\mathbf{v} \right\} d\lambda \tag{5.6}$$

The expression enclosed within the curly braces represents the van Cittert-Zernike theorem.

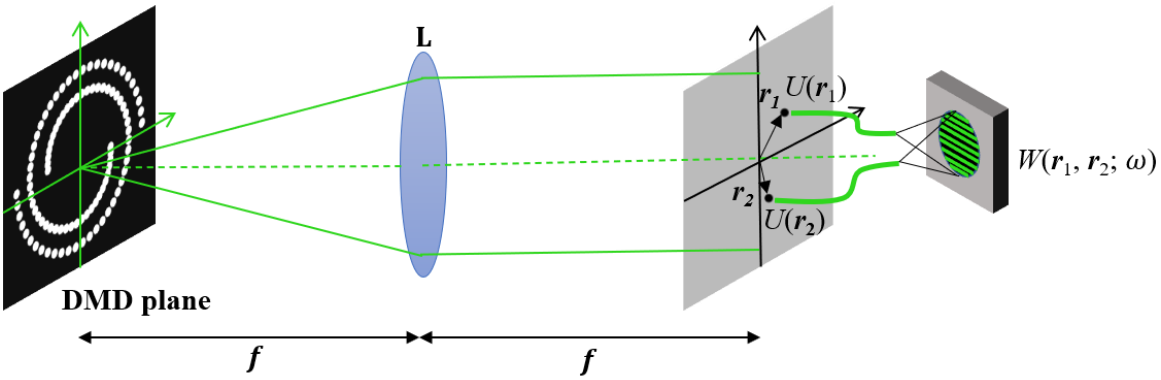

Fig. 5.2 Schematic diagram for recording two-point correlation function.

5.2.2 Experiment and results discussions

To experimentally measure the CVs, we used a Sagnac radial shearing interferometer as shown in Fig. 5.3. The setup begins with a green light-emitting diode (LED) source illuminating a wavelength filter via a high-magnification microscope objective (60x). This filter selects a light source centered around 535 nm, with a bandwidth of approximately 15 nm. Next, the diverging beam is collimated using a lens L1 with a focal length of 4.5 cm. The collimated beam is then directed onto a DMD, where binary pinhole patterns are displayed. The DMD reflects the modulated light pattern at an angle of +24° from the normal, and a mirror M1 aligns the beam along the desired optical path. The modulated beam is subsequently processed through a Fourier-transforming lens L2 with a focal length of 10 cm. At this stage, a polarizer P1 generates a diagonally polarized beam. The two-point correlation function is determined at the Fourier plane of the system. Now for the

measurement of the two-point correlation function the beam is directed into the Sagnac radial shearing interferometer. The diagonally polarized stochastic beam splits into two orthogonal *x* and *y* polarized components, through a polarizing beam splitter (PBS). Later, a cyclic path composed of three mirrors M2, M3 and M4 and a telescopic lens system L3 (focal length f_3 = 15 cm) and L4 (focal length f_4 = 20 cm) makes different magnifications of the counter propagating beams in the interferometer. Out of two counter propagating beams, one gets magnified with factor $\alpha = f_4/f_3$ and other gets demagnified with factor $\alpha^{-1} = f_3/f_4$. The coordinates of the Fourier domain are now scaled as $\boldsymbol{r}_1 = \alpha^{-1}\boldsymbol{r}$ and $\boldsymbol{r}_2 = \alpha\boldsymbol{r}$. As a result, we observe two sheared copies of the beams at the recording plane, introducing an in-plane radial shear $\Delta\boldsymbol{r} = (\alpha - \alpha^{-1})\boldsymbol{r}$. Before detection, we use a quarter-wave plate (QWP) to convert the *x*-polarized and *y*-polarized beams into right hand circularly polarized and left hand circularly polarized beams, respectively. Later a polarizer P2 is placed to make the two beams interfere and for introducing the phase shifts. Fig. 5.4 shows a laboratory picture of the experimental set up.

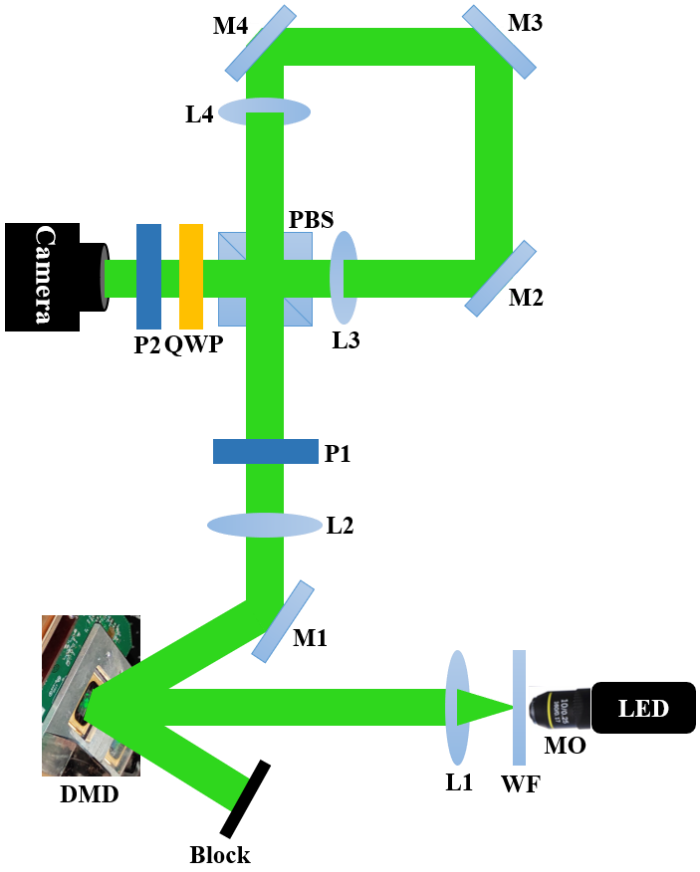

Fig. 5.3 Experimental set up: LED: Light Emitting Diode; WF: Wavelength Filter; L: Lens; DMD: Digital Micromirror Device; M: Mirror; P: Polarizer; PBS: Polarization Beam Splitter; QWP, Quarter Wave Plate.

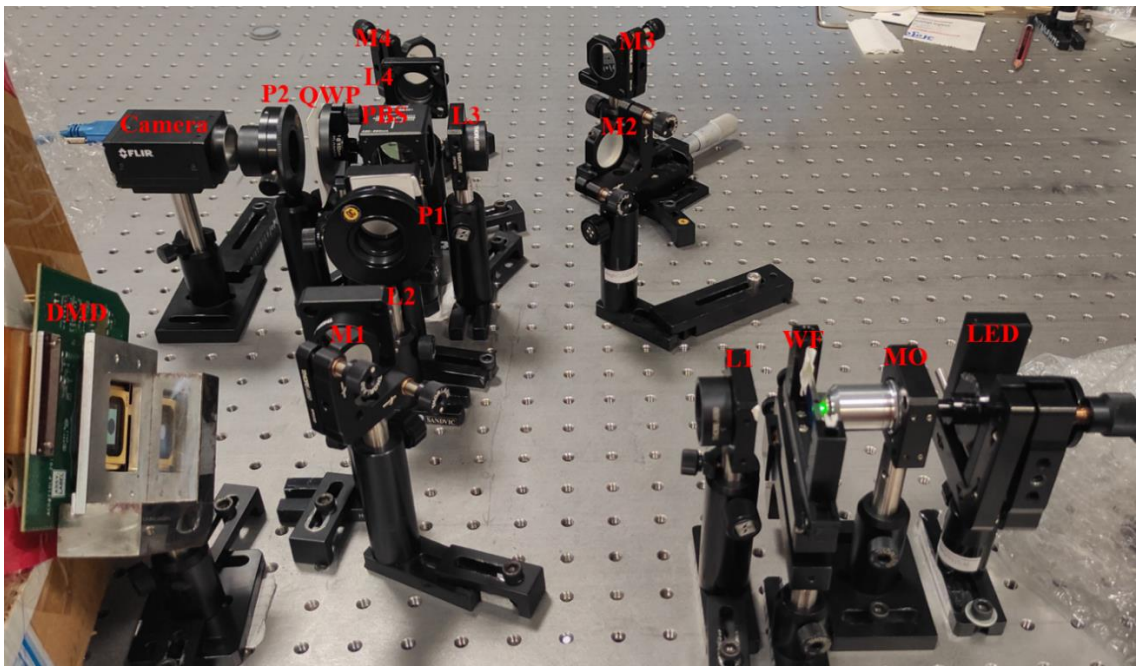

Fig. 5.4 Laboratory experimental setup.

Phase shifts of 0, π/2, π, and 3π/2 are introduced to create four interferograms $I(0)$, $I(\pi/2)$, $I(\pi)$, $I(3\pi/2)$, respectively. Fig. 5.5 shows the images of four experimentally recorded interferograms for two spirals case. These interferograms are utilized to calculate the fringe visibility (g) and the fringe phase (ϕ) using four-phase shifted algorithm [315]

$$g(\boldsymbol{r}_1, \boldsymbol{r}_2) \propto \frac{\sqrt{[I(0)-I(\pi)]^2+[I(\pi/2)-I(3\pi/2)]^2}}{I(0)+I(\pi/2)+I(\pi)+I(3\pi/2)}, \tag{5.7}$$

$$\phi(\boldsymbol{r}_1, \boldsymbol{r}_2) = tan^{-1}\left[\frac{I(3\pi/2)-I(\pi/2)}{I(\pi)-I(0)}\right], \tag{5.8}$$

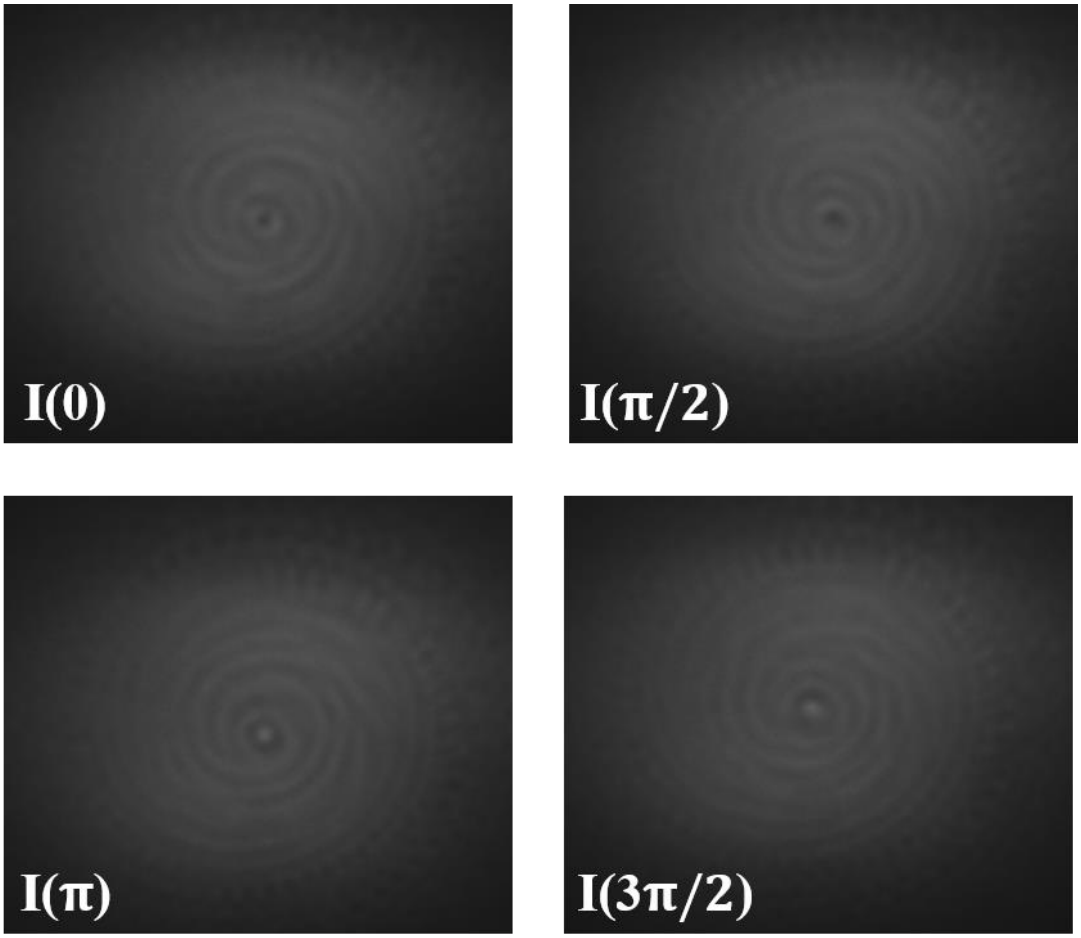

Fig. 5.5 Recorded interference patterns for two spirals with phase-shifts (a) 0, (b) π/2, (c) π, and (d) 3π/2.

Finally, using g and ϕ the two-point correlation function is recovered as

$$W(\alpha^{-1}\boldsymbol{r}, \alpha\boldsymbol{r}) = g(\alpha^{-1}\boldsymbol{r}, \alpha\boldsymbol{r})\, exp[i\phi(\alpha^{-1}\boldsymbol{r}, \alpha\boldsymbol{r})], \tag{5.9}$$

Here, the two-point correlation function's amplitude distribution is represented by the fringe visibility, and its phase distribution by the fringe phase.

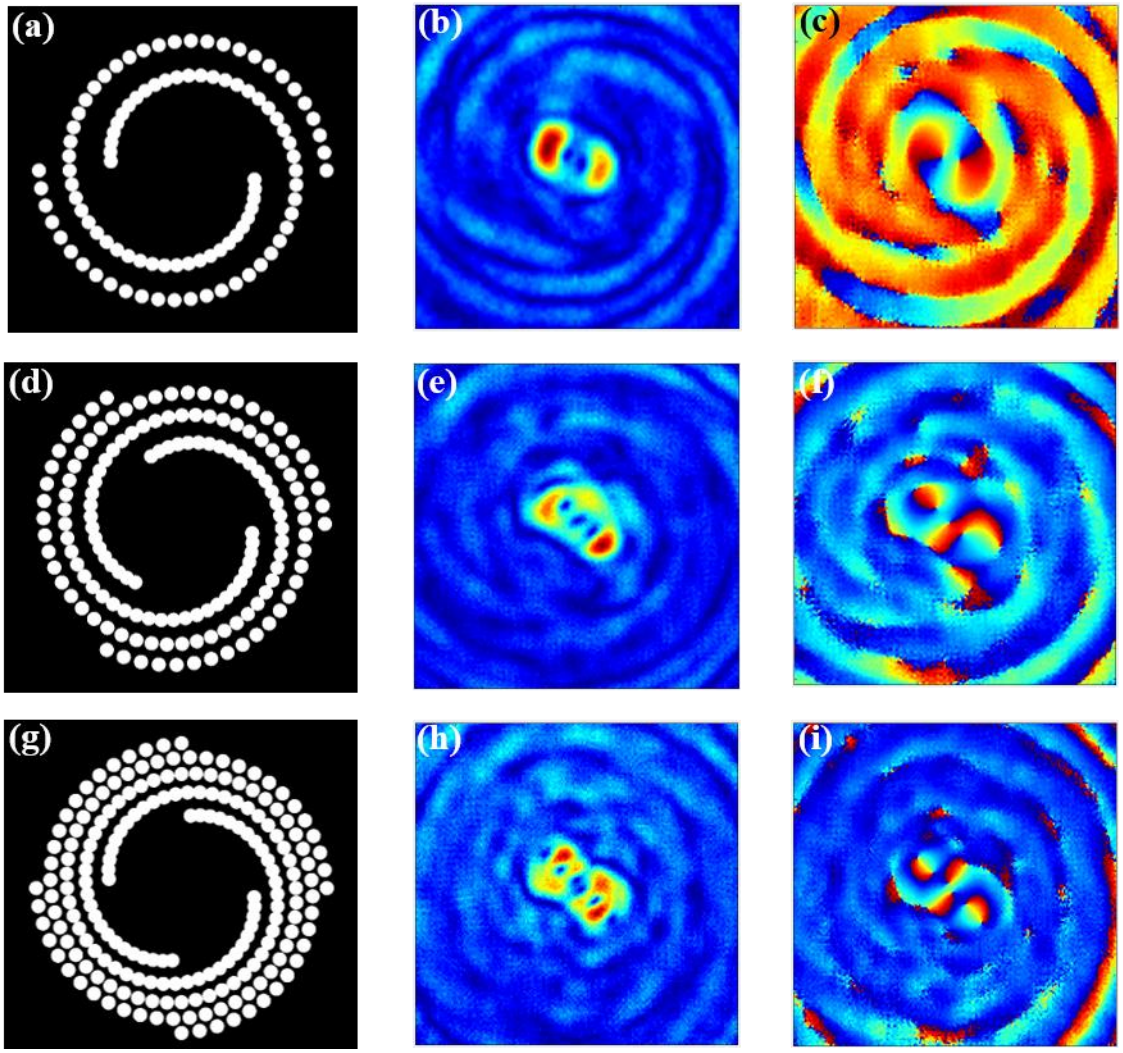

Fig. 5.6 Experimental results. (a) two spirals, (e) three spirals, and (i) four spirals; (b), (f), and (j) the corresponding absolute values of the two-point spatial coherence function; (c), (g), and (k) the corresponding phase values of the two-point spatial coherence function.

Figure 5.6 illustrates the experimental results demonstrating the generation of CVs. Panels (a), (d), and (g) depict the binary spiral pinhole apertures designed with two, three, and four spirals, respectively. The corresponding experimental results for the absolute values of the complex spatial coherence are presented in panels (b), (e), and (h), while the phase values of the complex spatial coherence are shown in panels (c), (f), and (i). The phase profiles distinctly reveal a helical structure, thereby confirming the presence of CVs. These results

validate the effectiveness of the binary spiral pinhole apertures in generating structured coherence properties, as reflected in both the magnitude and phase distributions of the spatial coherence.

5.3 Digital generation using SLM

This section demonstrates the generation of CVs using phase-type SLM. The theoretical foundation, experimental setup, and corresponding results are elaborated upon in the following sections. The method utilizes the orthogonal polarization basis of light to show the formation of CVs in complex two-point correlation function.

5.3.1 Theoretical background

Fig. 5.7 represents the configuration for inserting the vortex in complex two-point correlation function of the light. Here, the incoherent source illuminates the source. The source is represented by the orthogonal polarization components. The vortex phase is loaded into a horizontal polarization component of the light and the vertical polarization component remains intact. The CVs is recovered by measuring the two-point correlation of these two orthogonal polarization components of the light. Let $U_x(\mathbf{v}_1)$ represent an instantaneous *x*-polarized component of the stochastic field and $U_y(\mathbf{v}_2)$ represents an instantaneous *y*-polarization component of the stochastic field. The statistical property of the source is defined by second order correlation function as,

$$W(\mathbf{v}_1, \mathbf{v}_2) = \langle U_x^*(\mathbf{v}_1) U_y(\mathbf{v}_2) \rangle \tag{5.10}$$

where $\langle \quad \rangle$ represents the ensemble average.

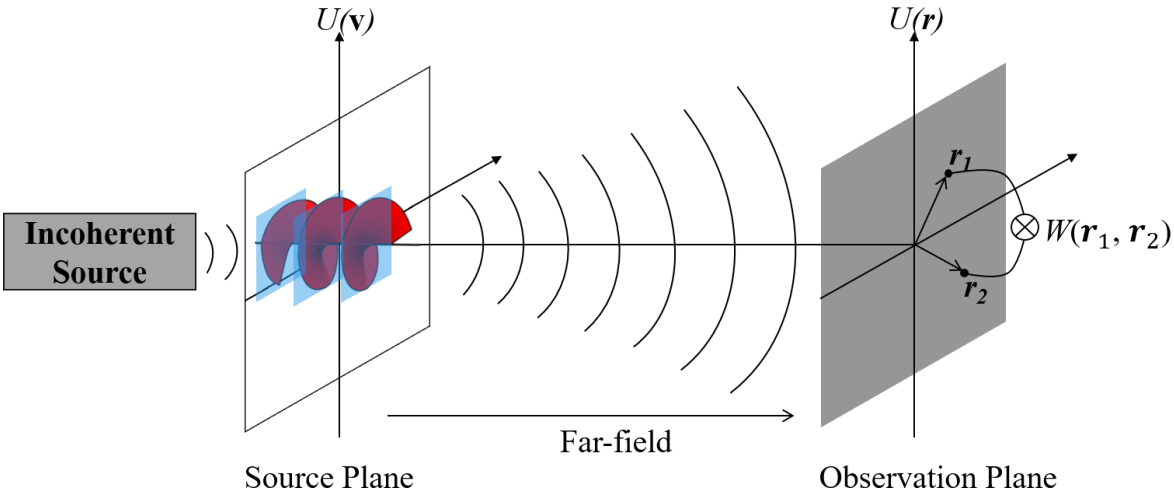

Fig. 5.7 Schematic diagram for recording two-point correlation function.

At the far-field, a single realization of these two orthogonal polarization fields is represented as

$$U'_n(\boldsymbol{r}) = \int U_n(\mathbf{v})\, exp\left(-i\frac{2\pi}{\lambda z}\mathbf{v}.\boldsymbol{r}\right) d^2\mathbf{v} \tag{5.11}$$

where $n = x, y$ represents the different orthogonal polarization components, λ denotes the wavelength of the source and z is the far-field distance. The two-point correlation function at the observation plane,

$$W(\boldsymbol{r}_1, \boldsymbol{r}_2) = \iint \langle U_x^*(\mathbf{v}_1) U_y(\mathbf{v}_2)\rangle\, exp\left[-i\frac{2\pi}{\lambda f}(\mathbf{v}_2.\boldsymbol{r}_2 - \mathbf{v}_1.\boldsymbol{r}_1)\right] d^2\mathbf{v}_2 d^2\mathbf{v}_1 \tag{5.12}$$

For an incoherent source,

$$\langle U_x^*(\mathbf{v}_1) U_y(\mathbf{v}_2)\rangle = I_{xy}(\mathbf{v})\delta(\mathbf{v}_2 - \mathbf{v}_1) \tag{5.13}$$

where $I_{xy}(\mathbf{v})$ is the source intensity and δ is a two-dimensional Dirac delta function.

Therefore, the far-field two-point correlation function is described as

$$W(\boldsymbol{r}_1, \boldsymbol{r}_2) = \int I_{xy}(\mathbf{v}) exp\left[-i\frac{2\pi}{\lambda f}(\boldsymbol{r}_2 - \boldsymbol{r}_1).\mathbf{v}\right] d^2\mathbf{v} \tag{5.14}$$

Eq. (5.14) represents the van Cittert-Zernike theorem, which defines the two-point correlation function as the Fourier transform of the incoherent source intensity distribution.

5.3.2 Simulation results

To illustrate the validation of our approach, we simulated far-field complex two-point spatial coherence function. We use phase transmittance function $\tau_x(\mathbf{v})$ for three different helical phase structure with TCs $l = 1$, $l = 2$, and $l = 1.5$.

Fig. 5.8 shows a schematic diagram of our simulation model along with a flow chart. In the simulation, the source plane comprised of horizontal and vertical polarization component transmittance functions $\tau_j(m,n)(j = x, y)$. This transmittance function is expressed as a 2D matrix with N × N discrete elements where, m and n are pixels, and x and y are orthogonal polarization components. For different polarization components, $\tau_j(m,n)$ is represented as

$$\tau_j(m,n) = \begin{cases} circ(m,n)exp\big(il\xi(m,n)\big), & m^2 + n^2 \le p^2, \ for\ j = x \\ circ(m,n) & ,m^2 + n^2 \le p^2, \quad for\ j = y \end{cases} \tag{5.15}$$

where $circ(m,n)$ is the circular function with radius pixels p. The helical phase transmittance function is inserted into the x-polarization component $\tau_x(m,n)$ where l is the TC and ξ represents the phase of the helical phase structure.

To simulate an incoherent light source, a random phase screen $\psi^k(m,n)$ is introduced into the source plane, where k represents a realization of the random phase screen. k varies from 1 to M, where M is the total number of random phase patterns. In the simulation, a phase screen $\psi^k(m,n)$ is a N×N array of random phase values. The phase of the random phase screen is uniformly distributed over the interval $[-\pi, \pi]$. Therefore, a single realization of the complex field at the source plane is represented as $U_j^k(m,n) =$

$\tau_j(m,n)exp[i\psi^k(m,n)]$. A discrete fast Fourier transform is applied to propagate the stochastic field to the observation plane. This process is executed for both orthogonal polarization components *i.e.*, $U_x^k(m,n)$ and $U_y^k(m,n)$. The resultant far-field is represented as $U_x'^k(m,n)$ and $U_y'^k(m,n)$. Correlation of the coherent random patterns is represented as $U_x'^{*k}(m_1,n_1)U_y'^k(m_2,n_2)$. This process is repeated for all M realizations $E'_j{}^1, E'_j{}^2, \ldots E'_j{}^M$ corresponding to different phase screens ψ^1, ψ^2,….ψ^M. The two-point spatial correlation function is obtained by averaging over all M random phase patterns. Following the simulation steps described above, we calculated two-point spatial correlation function of the fields.

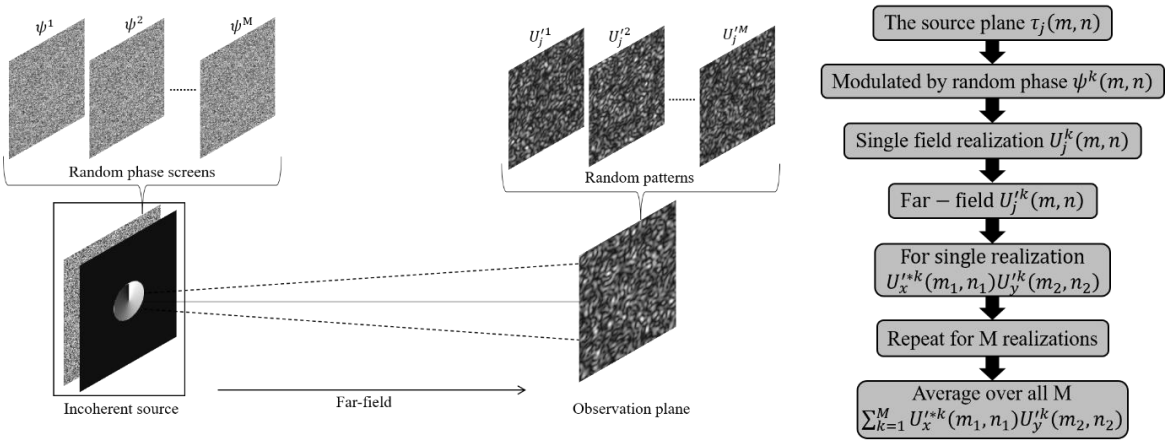

Fig. 5.8 Schematic illustration of the far-field with the corresponding flow chart.

Fig. 5.9 shows the simulation results obtained by considering helical phase with different TCs $l = 1$, $l = 2$, and $l = 1.5$. The first row in Fig. 5.9 shows the amplitude distribution of the complex spatial correlation function for (a) $l = 1$, (b) $l = 2$, and (c) $l = 1.5$. The second row shows the corresponding phase distribution of the correlation function for (d) $l = 1$, (e) $l = 2$, and (f) $l = 1.5$.

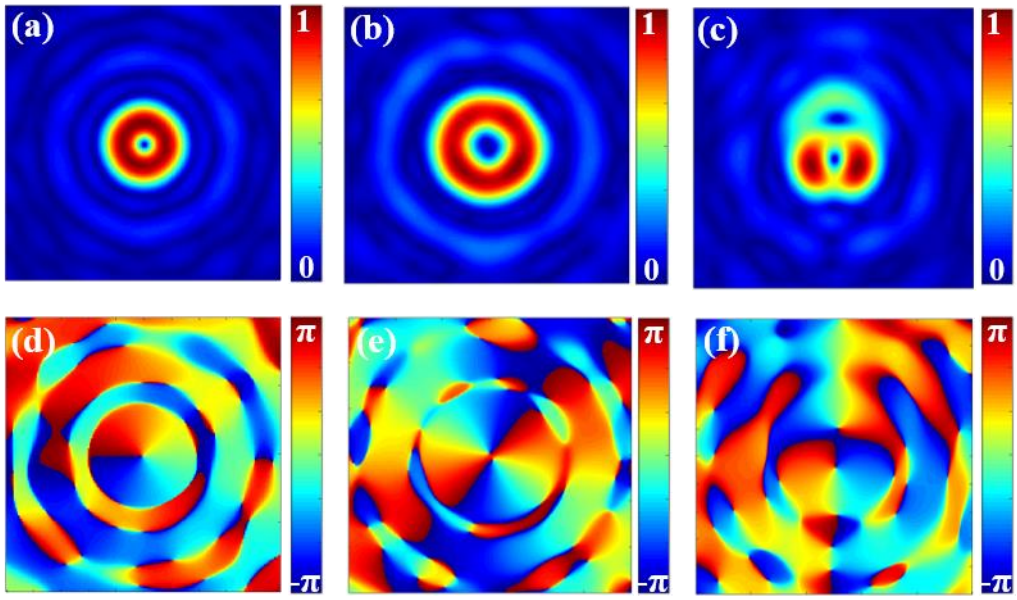

Fig. 5.9 Simulation results: Amplitude distribution of the complex correlation function for (a) $\boldsymbol{l = 1}$, (b) $\boldsymbol{l = 2}$, and (c) $\boldsymbol{l = 1.5}$. Phase distribution of the complex spatial correlation function for (d) $\boldsymbol{l = 1}$, (e) $\boldsymbol{l = 2}$, and (f) $\boldsymbol{l = 1.5}$.

5.3.3 Experiment and results discussions

Fig. 5.10 shows our experimental scheme which consists of two major parts. In Part I, a diagonally polarized thermal light source illuminates a reflective type phase only SLM (Holoeye, PLUTO-2.1 LCOS). This thermal light source is realized by illuminating a rotating ground glass (RGG) with a monochromatic light source (He-Ne laser of wavelength 632.8 nm). The SLM placed at the front focal plane of a lens L1 inserts helical phase with a transmission function $\tau(\mathbf{v})$ into the *x*-polarized component of the beam represented by a symbol $\odot$ and the *y*-polarized component, represented by symbol $\updownarrow$, remains intact. Thus, $U_x(\mathbf{v})$ represents a single realization of the stochastic field with the helical phase structure. Similarly, $U_y(\mathbf{v})$ represents a single realization of the stochastic field without helical phase structure. These two copies of the stochastic fields co-linearly propagate and reach the back focal plane of lens L1 with focal length f_1=250 mm, which is highlighted by the black dotted line in Fig. 5.10. According to Eq. (5.13), at the back focal plane of lens L1 we get the two-point spatial coherence function.

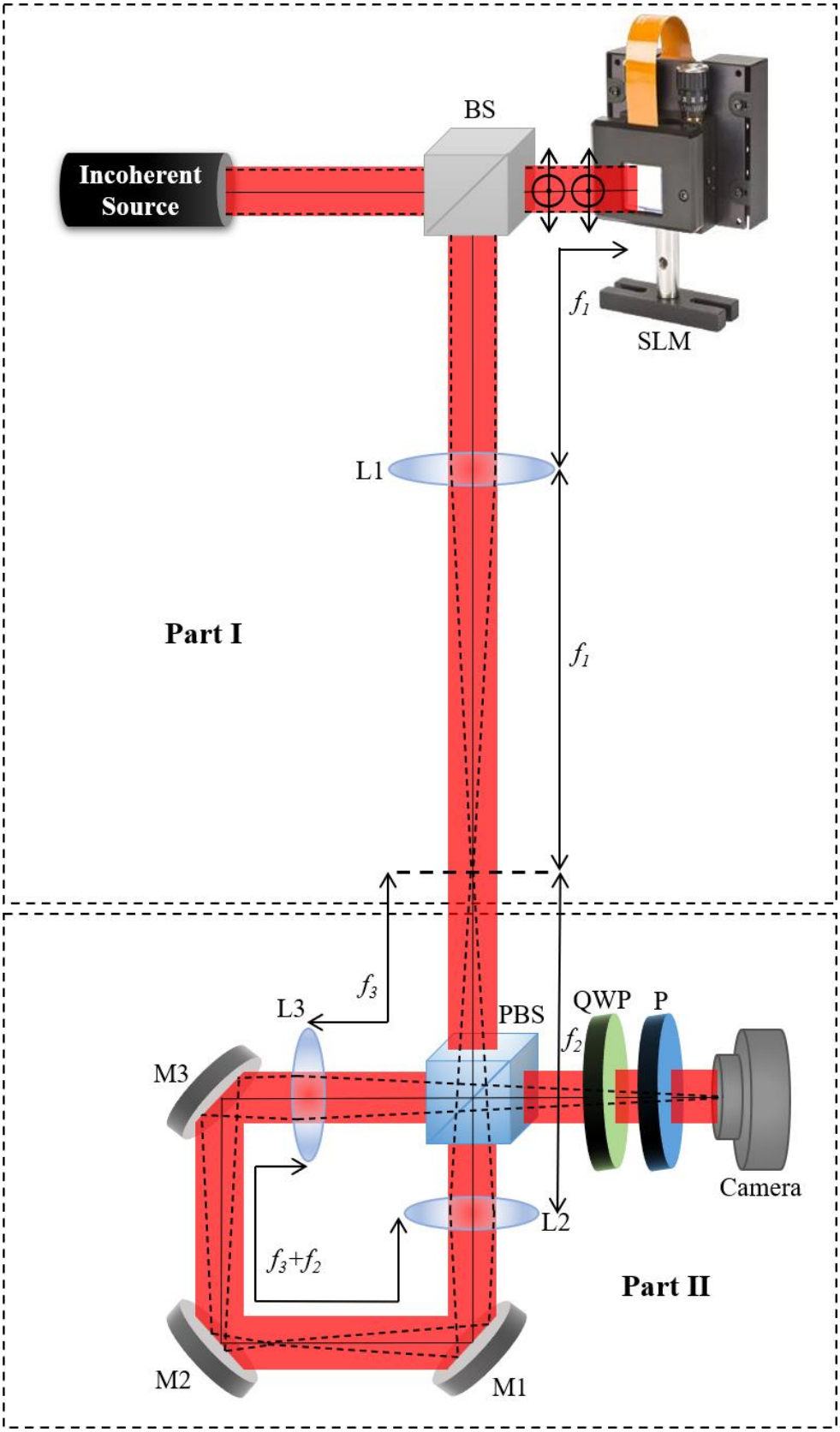

Fig. 5.10 Experimental setup square Sagnac radial shearing interferometer: L: lens, BS: beam splitter, SLM: spatial light modulator. PBS: polarization beam splitter, M: mirror, QWP: quarter wave plate, P: polarizer.

Now, in order to experimentally measure the complex two-point spatial correlation, we designed a cyclic Sagnac radial shearing interferometer as shown in Part II of Fig. 5.10. A diagonally polarized stochastic beam splits into two orthogonal horizontal and vertical polarization components by a polarizing beam splitter (PBS). An optical system comprised of mirrors M1, M2, and M3 along with PBS forms a cyclic path interferometer. The transmitted beam from PBS gets magnified with magnification factor $\alpha = f_3/f_2 = 1.143$ formed with telescopic lens system L2 and L3 with focal lengths f_2 =175 mm and f_3 =200 mm, respectively. Whereas, the reflected beam demagnified with factor $\alpha^{-1} = f_2/f_3 = 0.875$. Thus, we have two radially sheared copies of the beams at the camera plane and an in-plane radial shear is introduced. At any arbitrary position of the detector, we have two scaled copies of the fields with scaling $\alpha\boldsymbol{r}$ for the object beam and $\boldsymbol{r}/\alpha$ for without the object beam. The Sagnac interferometer is insensitive to external disturbances due to its common path configuration.

Since the field cannot be measured directly, a phase-shifting approach is applied to experimentally measure the two-point spatial correlation function from the interference patterns. A geometric phase shifter composed of a combination of a quarter-wave plate (QWP) and a polarizer (P) introduces the necessary phase shift into the interfering beams. A QWP kept at 45˚ from its fast axis along the x direction converts two orthogonal x and y polarized beams into right-circularly polarized and left-circularly polarized beams, respectively. A polarizer P is kept at an angle θ with respect to the horizontal axis. A single realization of the stochastic field emerging out of the QWP and polarizer is represented by the Jones matrix as [42]

$$\begin{pmatrix} U_x'(\boldsymbol{r}_1,t) \\ U_y'(\boldsymbol{r}_2,t) \end{pmatrix} = \frac{1}{\sqrt{2}} \begin{pmatrix} cos^2\,\theta & sin\theta\, cos\theta \\ sin\theta\, cos\theta & sin^2\,\theta \end{pmatrix} \begin{pmatrix} 1 & i \\ i & 1 \end{pmatrix} \begin{pmatrix} U_x(\boldsymbol{r}_1,t) \\ U_y(\boldsymbol{r}_2,t) \end{pmatrix} \tag{5.16}$$

Therefore, the average intensity at the detector plane is given as

$$I(\theta) = \langle (U_x'^*(\boldsymbol{r}_1, t) \quad U_y'^*(\boldsymbol{r}_2, t)) \begin{pmatrix} U_x'(\boldsymbol{r}_1, t) \\ U_y'(\boldsymbol{r}_2, t) \end{pmatrix} \rangle \tag{5.17}$$

$$I(\theta) \approx \frac{1}{2} \left[\langle U_x^2(\boldsymbol{r}_1) \rangle + \langle U_y^2(\boldsymbol{r}_2) \rangle + 2sin(2\theta) \langle U_x^*(\boldsymbol{r}_1) U_y(\boldsymbol{r}_2) \rangle \right] \tag{5.18}$$

where $I(\theta)$ is ensemble averaged intensity which is realized by making a number of stochastic field realizations due to RGG.

Eq. (5.18) represents interference patterns between two beams and a resultant phase-shift 2θ is introduced into the interfering beams by a geometric phase-shift scheme. Rotating a polarizer by an angle θ introduces a phase-shift 2θ between the two interfering beams. Four interferograms with phase-shifts 0, π/2, π, and 3π/2 are recorded and represented as $I(0), I(\pi/2),\ I(\pi)$ and $I(3\pi/2)$, respectively at the detector plane (Camera: CMOS-Thorlabs, Model No. DCC3240C). These interferograms are used to estimate the fringe visibility g and phase ϕ using the relation [43]

$$g \propto \frac{2\sqrt{\left(I(0) - I(\pi)\right)^2 + \left(I(\pi/2) - I(3\pi/2)\right)^2}}{I(0) + I(\pi/2) + I(\pi) + I(3\pi/2)} \tag{5.19}$$

$$\phi = \arctan\left[\frac{I(3\pi/2) - I(\pi/2)}{I(\pi) - I(0)}\right] \tag{5.20}$$

Therefore, the complex spatial correlation function is represented as

$$W(\Delta\boldsymbol{r}) = \ g(\Delta\boldsymbol{r})\ exp(i\ \phi(\Delta\boldsymbol{r})) \tag{5.21}$$

Fig. 5.11 shows the experimental results obtained by displaying different helical phase structures on SLM with TCs $l = 1$, $l = 2$, and $l = 1.5$. The first row in Fig. 5.11 shows the amplitude distribution of the complex spatial correlation function for (a) $l = 1$, (b) $l = 2$, and (c) $l = 1.5$. The second row shows the corresponding phase distribution of the

correlation function for (d) $l = 1$, (e) $l = 2$, and (f) $l = 1.5$. The experimental results (Fig. 5.11) are in good agreement with the simulation results (Fig. 5.9).

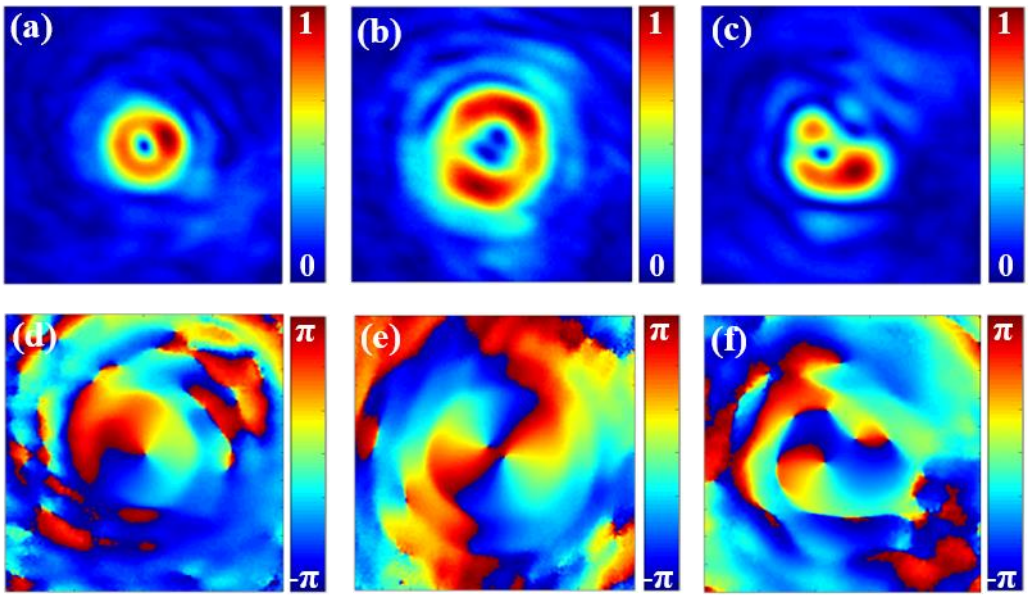

Fig. 5.11 Experimental results: Amplitude distribution of the complex correlation function for (a) $\boldsymbol{l = 1}$, (b) $\boldsymbol{l = 2}$, and (c) $\boldsymbol{l = 1.5}$. Phase distribution of the complex spatial correlation function for (d) $\boldsymbol{l = 1}$, (e) $\boldsymbol{l = 2}$, and (f) $\boldsymbol{l = 1.5}$.

5.4 Conclusion

In summary, we presented a novel approach for embedding helical phase structures into the two-point correlation function of a partially coherent beam, utilizing two advanced digital devices: DMD and SLM. The methodology is experimentally implemented and analyzed using a radial shearing interferometer. A comprehensive discussion of the underlying principles is provided, and the findings are validated through both simulations and experimental observations. The results distinctly showcase the characteristic features of CVs, evidenced by a dark core in the amplitude distribution and a helical phase structure in the phase profile of the complex two-point correlation function.